Electronic Supplementary Material (ESI) for Analytical Methods.

Supplementary information

Deep learning method for multi-task intelligent detection of oral cancer based on optical fiber Raman spectroscopy

Lianyu Li et al.

1. Raman Spectroscopy Analysis

Initially, we categorized all the Raman spectroscopy data by type and selected the spectroscopy data within the range of 400 - 4000 cm^{-1} for further analysis. Simultaneously, in order to avoid the problem of sample imbalance, we calculate the average Raman spectra of each class, and get a uniform spectrum. Before analyzing the spectral data, it is necessary to preprocess it in order to reduce the influence of robust fluorescence signal and noise brought by different background sources. This preprocessing phase consists of three steps:

(i) The Whittaker Smoother is utilized during signal denoising to smoothen the spectral data, hence reducing the effect of noise on the spectrum.

(ii) Following signal denoising, the double-weighted penalty-based least squares multiplication baseline correction method is employed for baseline correction to fit the polynomial baseline and eliminate the fluorescent background from the initial spectrum.

(iii) Lastly, data normalization is executed using maximum intensity normalization to standardize the intensity of all spectra within the [0,1] range, facilitating comparison among various samples.

Figs. 1 to 4 depict significant changes in Raman spectra between tumor staging (TI and TII), lymph node staging (N0 and N1), histological grading (MPD and WD), and between tumor and healthy tissue. Table 1 through 4 provides a comprehensive analysis of peak positions and assignments in Raman spectroscopy for tasks related to tumor staging, lymph node staging, and histological grading. For tumor staging, the 1050 Raman spectral data points from all oral cancer patients were categorized into TI and TII groups, consisting of 690 TI and 360 TII instances. Table 1 and Fig. 1 highlight the noticeable distinctions in the Raman spectra between TI and TII. Specifically, spectral peaks show an increase at 983 (Lipids), 1014 (Carbohydrates), 1206 (Hydroxyproline), 1220 (Amide III), 2550-2580 (ν(S-H) (aminoacid methionine)), and 3232 (O-H & N-H stretching vibrations) cm^{-1}. Conversely, decreases are observed at 484 (Glycogen), 585 (OH out of plane bending and phosphate of HA), 685 (DNA bases), 767 (Pyrimidine ring breathing mode), 799 (Phosphates), 858 (Tyrosine, collagen), 863 (Phosphatidic acid), 2741 (Stretching vibrations of CH, NH, and OH groups), 2800-3050 (Contributions from acyl chans), and 3300 (Attributed to OH stretch) cm^{-1}.

Lymph node staging was divided into N0 and N1 groups, comprising 750 cases of N0 and 300 cases of N1. Table 2 demonstrates the evident distinction between N0 and N1. Fig. 2 further details the Raman spectra differences, with increased peaks at 607 (Glycerol), 756 (Tryptophan), 815 (Tyrosine, proline, hydroxyproline,), 862 (Phosphate group), 988 (Proteins), 1195 (Nucleic acids and phosphates), 1210 (Phenylalanine), 1260 (Lipids), 1304 (Adenine, cytosine), and 1366 (Tryptophan) cm^{-1}. Decreases in spectral peaks are noted at 429 (Cholesterol), 2550-2580 (ν(S-H) (aminoacid methionine)), 2987 (Cholesterol ester), 3006 (Bond=C-H stretch), 3015 (ν=CH of lipids), and 3296 (Amide A) cm^{-1}.

Finally, histological grading divided tumor patients into WD and MPD groups, with 840 WD and 210 MPD cases. The distinctions between these groups are evident in Table 3 and Fig. 3. Notable changes are observed at 1174 (Phenylalanine), 1198 (Tryptophan), 1220 (Amide III), 1223 (Collagen I), 1437 (Acyl chains), and 3232 (O-H & N-H stretching vibrations) cm-1. Conversely, decreases are noted at 484 (Glycogens), 516 (Phosphatidylinositol), 719 (Phospholipid), 728 (Collagen), 815 (Nucleic acid), 820 (Structural protein modes of tumors), 858-863 (Tyrosine, collagen type I), 2741 (Stretching vibrations of CH, NH, and OH groups), and 2800-3100 (CH, CH2) cm^{-1}.

Furthermore, Fig. 4 and Table 4 present the results of Raman spectral analysis between normal and tumor tissues, highlighting increased spectral peaks at 962 (Phoisphate symmetric stretching vibration of calcium hydroxyapatite), 1034 (Phenylalanine of collagen), 1131 (Phenylalanine, C-N stretching of proteins), 1216 (Stretching of C-N), 1304 (Adenine, cytosine), 1437 (Acyl chains), and 3232 (O-H & N-H stretching vibrations) cm^{-1}. Decreases are observed at 445 (N-C-S stretch), 484 (Glycogen), 524 (S-S disulfide stretching in proteins), 802 (Uracil based ring breathing mode), 859 (Tyrosine, collagen), 2741 (Stretching vibrations of CH, NH, and OH groups), and 2800-3100 (CH, CH_2) cm^{-1}. These findings contribute to a comprehensive understanding of the Raman spectral characteristics in different pathological contexts.

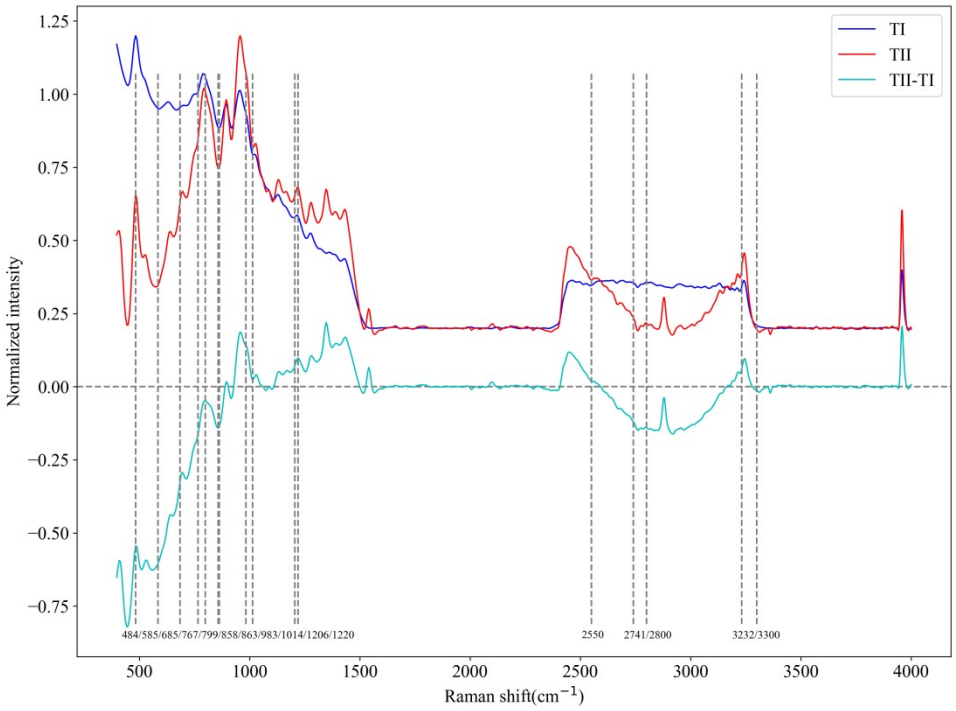

Fig. 1. The Raman Spectra of Oral Cancer Tissues Across Varying Tumor Staging (with preprocessing).

Table 1: Analysis of Peak Positions and Assignment in Raman Spectra under the tasks of Tumor Staging.

Progression type	Change direction	Raman shift (cm^{-1})	Band assignments
TII-TI	Increase	983	Lipids
		1014	Carbohydrates
		1206	Hydroxyproline
		1220	Amide III
		2550-2580	ν(S-H) (aminoacid methionine)
		3232	O-H & N-H stretching vibrations
	Decrease	484	Glycogen
		585	OH out of plane bending and phosphate of HA

		685	DNA bases
		767	Pyrimidine ring breathing mode
		799	Phosphates
		858	Tyrosine, collagen
		863	Phosphatidic acid
		2741	Stretching vibrations of CH, NH, and OH groups
		2800-3050	Contributions from acyl chans
		3300	Attributed to OH stretch

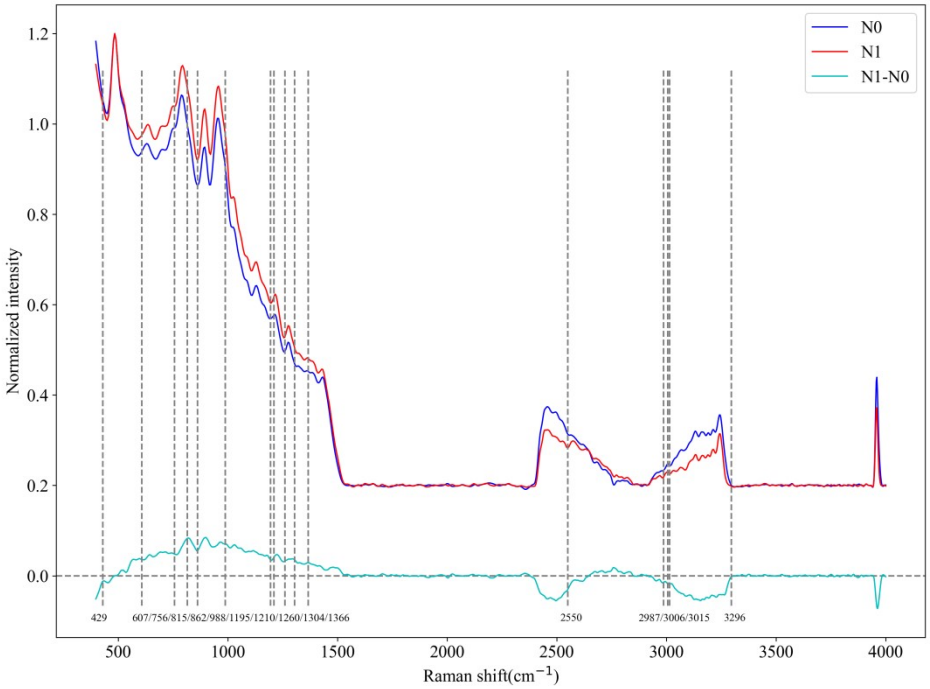

Fig. 2. The Raman Spectra of Oral Cancer Tissues Across Varying Lymph Node Staging (with preprocessing).

Table 2: Analysis of Peak Positions and Assignment in Raman Spectra under the tasks of Lymph Node Staging.

Progression type	Change direction	Raman shift (cm^{-1})	Band assignments
N1-N0	Increase	607	Glycerol
		756	Tryptophan
		815	Tyrosine, proline, hydroxyproline,
		862	Phosphate group
		988	Proteins
		1195	Nucleic acids and phosphates

		1210	Phenylalanine
		1260	Lipids
		1304	Adenine, cytosine
		1366	Tryptophan
	Decrease	429	Cholesterol
		2550-2580	ν(S-H) (aminoacid methionine)
		2987	Cholesterol ester
		3006	Bond=C-H stretch
		3015	ν=CH of lipids
		3296	Amide A

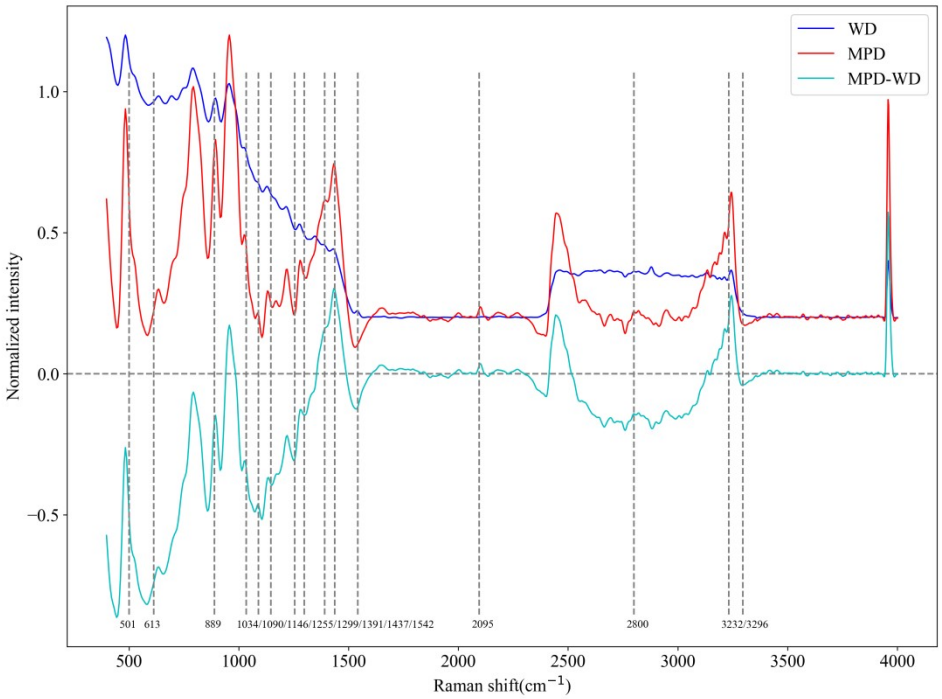

Fig. 3. The Raman Spectra of Oral Cancer Tissues Across Varying Histological Grading (with preprocessing).

Table 3: Analysis of Peak Positions and Assignment in Raman Spectra under the tasks of Histological Grading.

Progression type	Change direction	Raman shift (cm^{-1})	Band assignments
MPD-WD	Increase	1391	CH rocking
		1437	Acyl chains
		2095	C-N stretch
		3232	O-H & N-H stretching vibrations
	Decrease	501	Methoxy group
		613	Cholesterol ester
		889	Methylene rocking
		1034	Phenylalanine of

			collagen
		1090	Phosphate
		1146	Carbohydrates
		1255/1299	Lipids
		1542	Amide II
		2800-3100	CH, CH_2
		3296	Amide A

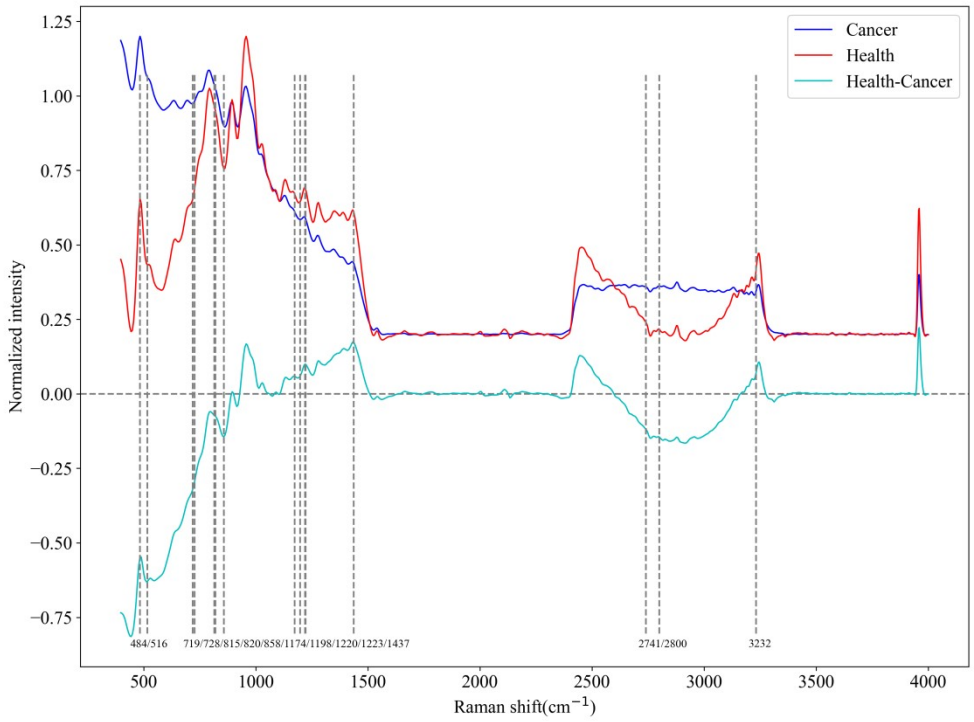

Fig. 4. The Raman Spectra of Oral Cancer Tissues Across Tumor and Health(with preprocessing).

Table 4: Analysis of Peak Positions and Assignment in Raman Spectra between Tumor and Health tissue.

Progression type	Change direction	Raman shift (cm^{-1})	Band assignments
Health-Cancer	Increase	1174	Phenylalanine
		1198	Tryptophan
		1220	Amide III
		1223	Collagen I
		1437	Acyl chains
		3232	O-H & N-H stretching vibrations
	Decrease	484	Glycogens
		516	Phosphatidylinositol
		719	Phospholipid
		728	Collagen
		815	Nucleic acid
		820	Structural protein modes of tumors

		858-863	Tyrosine, collagen type I
		2741	Stretching vibrations of CH, NH, and OH groups
		2800-3100	CH, CH2

2. MTN-AlexNet

In this section, we gain a deeper understanding of the predictive accuracy and misclassification associated with the MTN-AlexNet model across different classification categories. A cumulative confusion matrix, presented in Fig. 5, summarizes the results of the 6-fold cross-validation performed. The model showed consistent accuracy in tumor stage classification. This is evidenced by the correct classification of 456, 215, and 461 cases as TI, TII, and Health respectively. The model similarly displayed high precision in the lymph node staging classification task, successfully identifying 469 cases as N0, 235 cases as N1, and 468 cases as Health. Finally, for the histologic grading classification task, the network model achieved correct classification results, identifying 610 cases as WD, 105 cases as WPD, and 479 cases as Health.

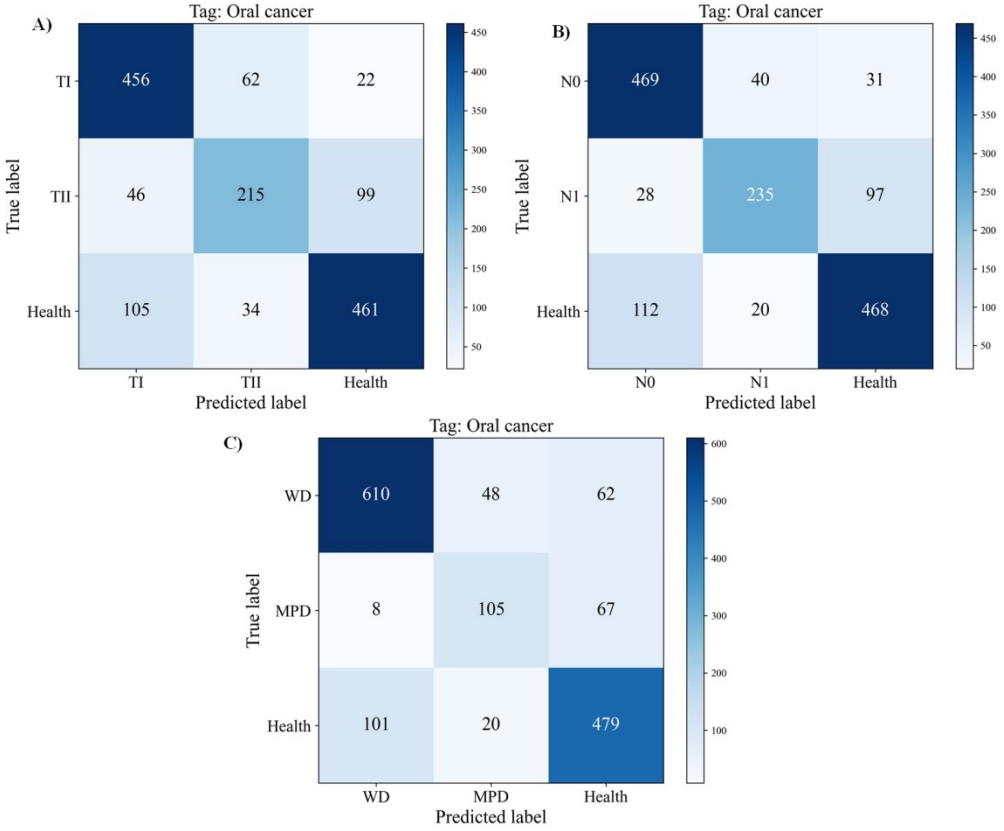

Fig. 5. Cumulative confusion matrix of 6-fold cross-validation corresponding to the MTN-AlexNet model on classification tasks covering tumor staging, lymph node staging, and histologic grading. (A) tumor staging task; (B) lymph node staging task; (C) histologic grading task.

3. MTN-GoogleNet

In Fig. 6, the cumulative confusion matrix obtained by six-fold cross validation illustrates the performance of the MTN-GoogleNet model across three distinct classification tasks. For the tumor

staging classification, MTN-GoogleNet performed well, categorizing 414, 214, and 455 cases as TI, TII, and Health, respectively. Similarly, in the lymph node staging classification, the model showcased precision by correctly classifying 413, 250, and 469 cases as N0, N1, and Health, respectively. For the histologic grading classification task, the model identified 635 cases as WD, 102 cases as WPD, and 469 cases as Health.

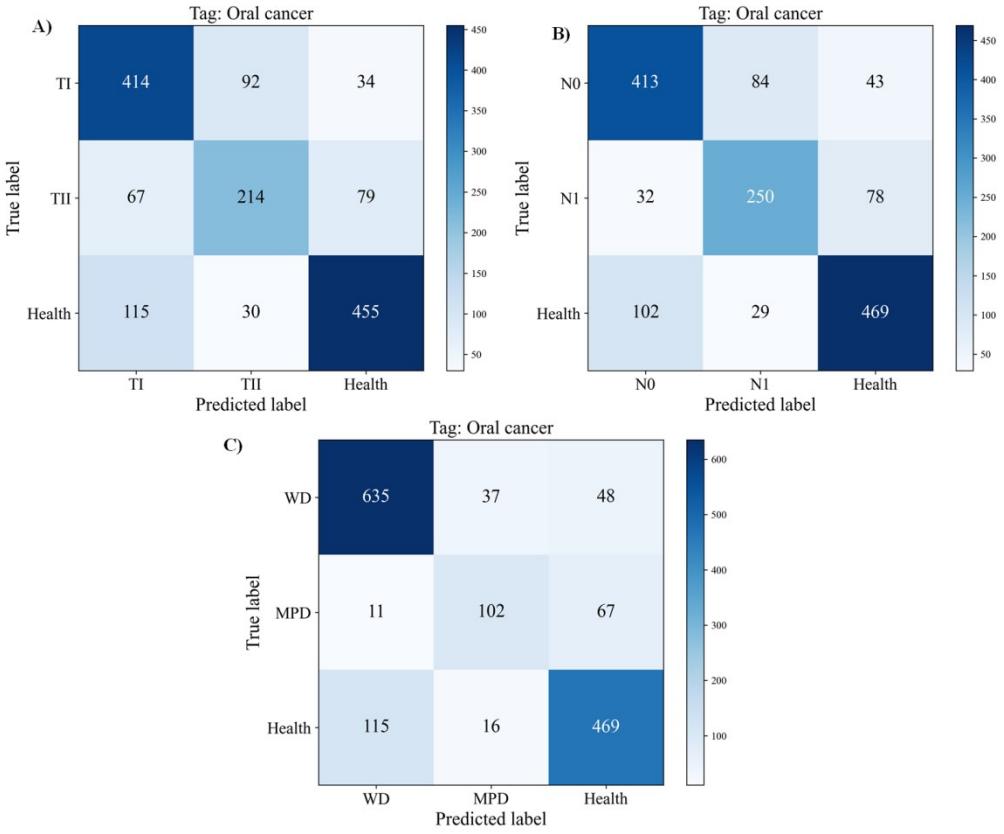

Fig. 6. Cumulative confusion matrix of 6-fold cross-validation corresponding to the MTN-GoogleNet model on classification tasks involving tumor staging, lymph node staging, and histologic grading. (A) tumor staging task; (B) lymph node staging task; (C) histologic grading task.

4. MTN-ResNet50

Fig. 7 showcases three distinct confusion matrices associated with the MTN-ResNet50 model, corresponding to the tumor staging, lymph node staging, and histological grading tasks. These matrices reveal the accuracy of the model in its classification: within the domain of tumor staging, the model recognized 415 cases as TI, 153 as TII, and 480 as Health. In the range of lymph node staging, the MTN-ResNet50 model shows that 427 cases as N0, 189 as N1, and 494 as Health. For histological grading, the model identified 557 cases of WD, 105 cases of WPD, and significant 486 cases of Health.

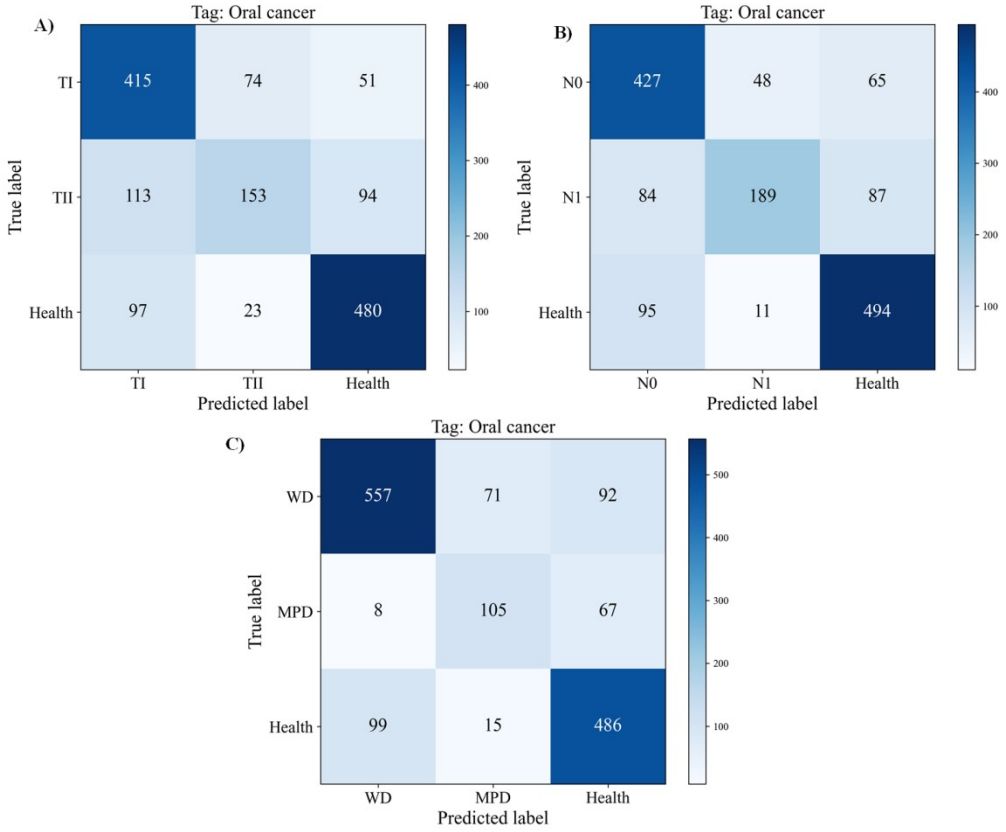

Fig. 7. Cumulative confusion matrix of 6-fold cross-validation corresponding to the MTN-ResNet50 model on classification tasks encompassing tumor staging, lymph node staging, and histologic grading. (A) tumor staging task; (B) lymph node staging task; (C) histologic grading task.

5. MTN-Transformer

Fig. 8 provides a graphical representation in the form of a cumulative confusion matrix, dividing the results of the three different classification tasks according to the six-fold cross validation. This visualization aims to measure the precision of the prediction and detect any errors in various categories. The results shown in Fig. 11 show that in the tumor stage classification process, the network model misclassified 72 cases as TI, 106 cases as TII, and 100 cases as Health. In the lymph node staging task, the model mislabeled 86 patients as N0, 102 as N1, and 92 as Health. On histological classification, MTN-Transformer incorrectly classified 87 cases as WD, 77 as MPD, and 91 as Health.

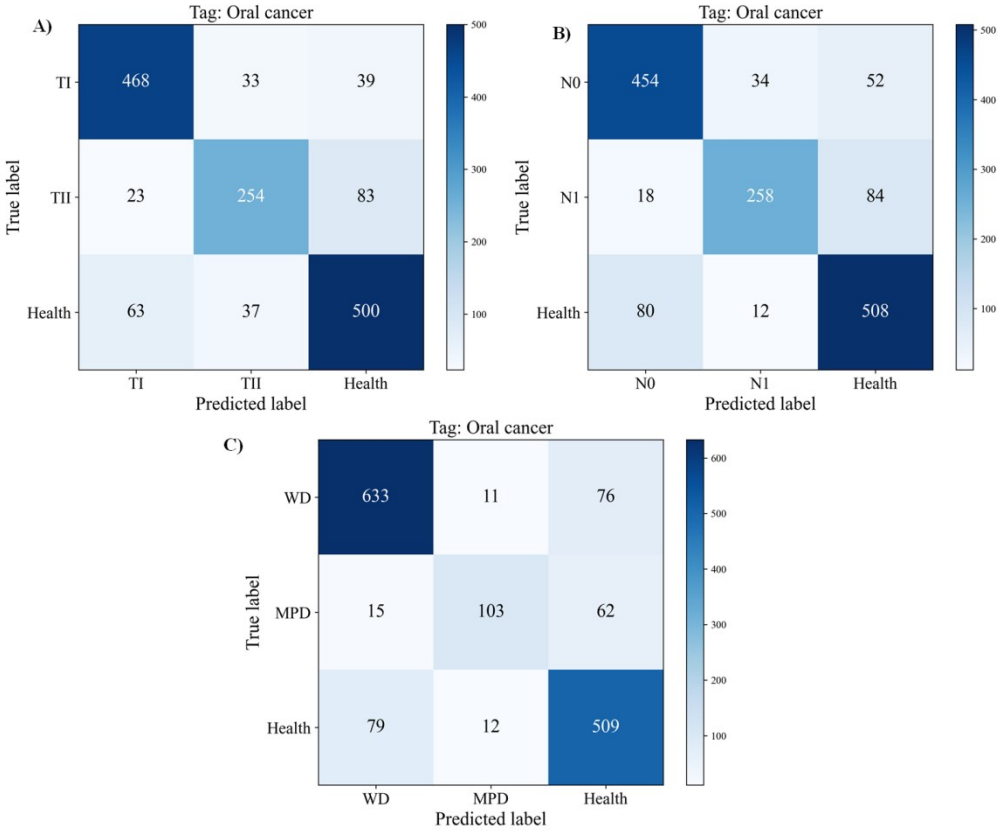

Fig. 8. Cumulative confusion matrix of 6-fold cross-validation corresponding to the MTN-Transformer network model on classification tasks involving tumor staging, lymph node staging, and histologic grading. (A) tumor staging task; (B) lymph node staging task; (C) histologic grading task.